Original Article

Research on microstructure and properties of Ti-based coating prepared by laser cladding on titanium alloy: simulation and experiment

Yanan Liu [a,1], Yue Wang [b,1], Xuejiao Yang [c], Peng Peng [c], Jichang Xie [d], Hyeong Kwang Benno Park [b], Yun Hwan Joo [b], In Wha Jeong [e,*], Tae Hyun Sung [b,**], Liangliang Xu [b,***]

[a] School of Mechatronics Engineering, Harbin Institute of Technology, Heilongjiang, Harbin 150001, China
[b] Department of Electrical Engineering, Hanyang University, Seoul 04763, South Korea
[c] School of Mechanical Engineering, Tiangong University, Tianjin 300387, China
[d] Laboratoire Roberval, FRE UTC-CNRS 2012, Sorbonne Universités, Université de Technologie de Compiègne, Centre de Recherche Royallieu, CS60319, 60203 Compiègne Cedex, France
[e] Department of Electrical Engineering, Dong-A University, Busan 49315, Republic of Korea

ARTICLE INFO

ABSTRACT

The heat transfer and solidification characteristics significantly affect the solidified microstructure of direct laser deposited coatings. In this work, a Ti-based coating was prepared on the Ti811 alloy by coaxial laser cladding to reveal the in-situ synthesis mechanism of the reinforcing phase and enhance its mechanical properties. The heat transfer evolution and solidification characteristics of the molten pool were investigated by numerical simulations and experiments. The phase composition, microstructure, interface characteristics, nano-hardness, and tribological properties of the deposited coating were studied. The results showed that the sufficient temperature of the molten pool ensured the formation of a deposited coating. The Marangoni convection of the molten pool facilitated the powder particles melting process as well as the uniformity of the reinforcing phase distribution. In addition, the temperature gradient and solidification rate at the upper of the solidified interface increased 2.27 and 29 times, respectively, compared to those at the bottom of the solidified interface. Thermodynamic and simulation results determined the precipitation sequence and mechanism of the phases. Due to the solid solution strengthening, dispersion strengthening effects, and robust interfacial bonding between phases, the nano-hardness of the deposited coating was 2.5 times higher than the substrate. Compared to the Ti811 alloy, the friction coefficient of the coating was reduced by around 30%. The tribological properties of the deposited coating dramatically improved, and the

---

* Corresponding author.
** Corresponding author.
*** Corresponding author.
E-mail addresses: jeongi@uci.edu (I.W. Jeong), sungth@hanyang.ac.kr (T.H. Sung), xuliang@hanyang.ac.kr (L. Xu).
[1] Co-first authors.

wear mechanism was mainly abrasive wear. This work theoretically and experimentally revealed the primary mechanism of in-situ enhancement to protect titanium alloys.

1. Introduction

Titanium alloys, with attractive mechanical properties such as high specific strengths, low densities, and excellent corrosion resistance, are important structural materials in the aerospace, machinery, metallurgy, and chemical industries [1—3]. However, their low hardness and terrible wear properties hinder their further applications [4—6]. Over the past few decades, numerous studies have been devoted to improving the surface properties of titanium and its alloys, such as laser cladding [7—9], plasma transferred arc welding [10], chemical/physical vapor deposition [11,12], and ion implantation [13]. Among these, laser cladding is considered one of the most effective surface modification technologies for preparing one or more layers on a substrate surface. Moreover, the high energy density and cooling rate can create a refined microstructure, controllable dilution ratio, and a robust metallurgical combination with the substrate to prevent delamination [14,15].

The laser cladding composite coating contains numerous interfaces, which act as a bridge connecting the reinforced phase and the substrate, playing an essential role in the mechanical properties of the coating [16,17]. The interface bonding between the reinforcing phases can be divided into mechanical and chemical bonding in the laser cladding composite coatings [18,19]. Mechanical bonding indicates that there is no chemical connection between the reinforced phase and the matrix, resulting in a poor bonding strength, which is essentially weak. However, the chemical bonding refers to the direct bonding between the reinforced phase through chemical bonds, leading to the ideal type of interface bonding in the composite coating, which is an effective interface bonding mode, such as the interface of La_2O_3/TiB [20], Ti_2AlN/TiAl [21], and $Ti_2Al(C, N)$/TiAl [22]. The robust bonding interface is an effective medium that transfers the load from the matrix to the reinforced phase, and its bonding strength has an important influence on the load transfer and strengthening mechanism [23]. Therefore, the study on the interfacial relationships of reinforced phases is of great importance for the design and preparation of high-performance composite coating and has always been an essential topic in materials research [24].

The interface investigation of the enhanced phase in laser cladding composite coatings mostly includes two aspects: orientation relationship and interface structure [25]. The orientation relationship describes the parallel crystal planes on both sides of the interface and their arrangement relationship, which is particularly important for revealing the formation mechanism of the composite coating [26]. Significantly, the reinforcing phases of composite coatings with higher interfacial bonding strength usually have a specific orientation relationship. Moreover, the interface structure mainly depends on the bond strength, stability, and lattice misfit [27,28]. Hu et al. [29] synthesized Ni_3Ta—TaC reinforced Ni-based wear-resistant coatings on 5Cr5MoSiV steel by laser cladding technology. Their results showed that the orientation relationship of TaC(100)//TiC(100) was determined by EBSD and TEM analysis, and the high adhesion and great stability of the interface were proved by the first principles calculation. Kooi et al. [30] demonstrated that the cracks in the B27 core of the TiB plate could be bridged and prevented by the Ti particles in the TiB/Ti composite coating prepared by laser cladding on TC4 alloy, which was beneficial to the improvement of tribological properties. Moreover, the combination of TiB with Ti and their appropriate spatial distribution promoted the fracture toughness, and the hardness was 2.78 times higher than the substrate.

Based on the discussion above, the composite coating prepared by laser cladding technology can form a strong metallurgical bond with the substrate. Furthermore, the high interfacial bonding strength between the reinforced phases endows its excellent mechanical properties. However, due to the typical non-equilibrium processing and the extremely fast melting and cooling rate characteristics of laser cladding, leading to relatively high requirements of the temperature evolution for in-situ reactions, which is an important issue in the laser cladding process [14,15,31]. Furthermore, laser cladding is a typical dynamic physical metallurgical process with complex multi-field coupling phenomena [31]. Recently, researchers have studied the interactions between lasers and materials to optimize and control the laser cladding process, eliminate the number of defects, and enhance the mechanical properties of the deposited coatings. In addition, simulation models have been used to improve the efficiency of exploring the laser process and powder material system. For example, a three-dimensional laser cladding model established by Chen et al. [32] was used to analyze the heat and mass transfer process of the Fe-based coating, which was used to accurately and reasonably describe the dynamic evolution of the molten pool. In another example, Wang et al. [33] simulated the interactions between the laser and powder material using a multiphysics model to accurately predict the geometry, heat transfer, and solidification characteristics of the molten pool for various parameter values during coating deposition on an Inconel 718 superalloy, which effectively reduced the optimized processing cost. Furthermore, to describe the microstructural characteristics of different areas of a laser cladding coating based on experimental and theoretical aspects, Li et al. [34] established a multiphysics model of a Fe60-based laser cladding coating prepared on an ASTM 1045 substrate. This approach accurately described the temperature evolution, velocity field, mass transfer, and solidification characteristics of the molten pool. At present, it is immature to study the growth mechanism of the reinforced phase and its interfacial relationship through the combination of experiment and simulation methods, which increases the difficulty of preparing laser cladding composite coatings by in-situ reactions.

Therefore, studying the interface structure, the heat transfer, and solidification characteristics of the molten pool are of great significance for investigating the microstructure evolution and in-situ growth reaction mechanism [35].

To this end, in this present work, a surface coating was deposited on the Ti811 alloy by the coaxial laser cladding technique. First, the heat transfer and solidification characteristics of the molten pool were studied through a combination of simulations and experiments, and the microstructural evolution characteristics of the coating were explored. Second, the in-situ reaction mechanism during the laser cladding process was studied based on the thermodynamic calculations and a simulation model. Finally, the interface characteristics and mechanical properties of the coating were studied. This study sheds light on the fundamental heat transfer and solidification characteristics of the molten pool and the in-situ formation mechanisms elucidated through theoretical and experimental methods of laser cladding coatings on titanium and its alloys.

2. Numerical simulations

Laser cladding is a typical dynamic physical metallurgical process consisting of complex multi-field coupling phenomena and interactions that involve the laser, powder, and workpiece [36,37]. First, a high-density laser beam was focused and radiated on the Ti811 alloy. Then, the powder flowed into the molten pool by gravity, delivering airflow and subsequently interacting with the laser beam to form a deposited coating on the substrate, and a solid/liquid phase transition occurred. Due to the surface tension gradient, Marangoni convection developed on the molten pool interface, causing the elements to be distributed evenly in the molten pool. As the laser beam moved away, the molten pool solidified, and a reinforced coating was deposited on the Ti811 alloy. Thus, a finite element model was established to simulate the transient process based on the COMSOL Multiphysics® software. Due to the symmetry of the molten pool, only half of the geometric model was established, where the dimensions of the model were $12 \times 5 \times 4$ mm^3, as shown in Fig. 1, and the maximum and minimum mesh sizes of this region were 0.18 and 0.018 mm, respectively. All symbols in
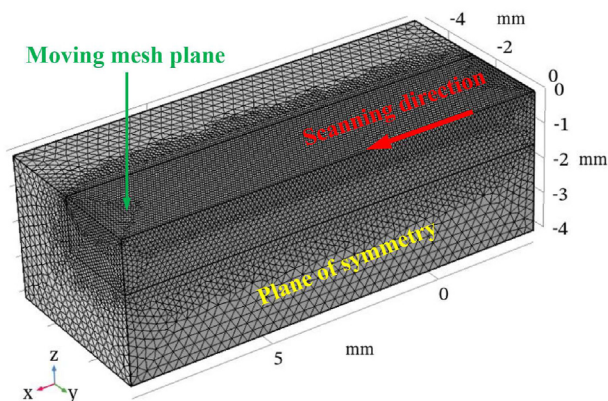
Table 1 – Nomenclature of symbols.	
Nomenclature	
A	mushy zone constant [kg/(m^3*s)]
B	a small number to prevent division by zero
c	specific heat capacity [J/(kg*K)]
F_l	liquid fraction of the metal phase
F_p	volume fraction of the powders
F_s	volume fraction of the substrate
K	thermal conductivity [W/(m^2*K)]
κ	curvature of gas–liquid interface
L	latent enthalpy content of the fusion [J/mol]
L_h	latent heat [J/mol]
N	the number of extranuclear electron layers of material atoms
$\boldsymbol{n}$	vector normal to the local free surface
$\boldsymbol{I}$	identity tensor
P	laser power [W]
p	pressure [Pa]
Q	heat source, W m^{-3}
R	effective radius of the laser spot [m]
R_e	electrical resistivity [Ω*m]
R_c	mass flow radius [m]
t	time [s]
T	temperature [K]
T_{amb}	room temperature [K]
T_l	liquidus temperature of metal [K]
T_s	solidus temperature of metal [K]
σ_b	Stefan–Boltzmann constant [W/(m^2*K^4)]
$\boldsymbol{u}$	flow velocity at liquid/gas interface [m/s]
V_m	mass flow rate [m/s]
W_m	material properties of the molten pool
W_p	material properties of the powders
W_s	material properties of the substrate
α	absorptivity
γ	heat transfer coefficient [W/(m^2*K)]
ε	radiation emissivity
η	powder catchment efficiency
λ	laser wavelength [m]
ρ	density [kg/m^3]
ρ_r	density of raw materials [kg/m^3]
σ	surface tension [N/m]
μ	viscosity [Pa*s]
$\boldsymbol{z}$	unit vector in the z direction

the following equations are listed in Table 1, and the following assumptions were made [38,39].

(1) The liquid metal in the molten pool is supposed to be Newtonian fluid, laminar fluid and incompressible fluid.
(2) The laser beam energy and powder flow concentration followed Gaussian distributions, where the heat source (Q) at the liquid/gas interface was defined by [40]:

$$Q = \frac{2\alpha(T)P}{\pi R^2}\exp\left[-2\frac{(x-v\cdot t)^2 + y^2}{R^2}\right] - \gamma(T - T_{abm})$$
$$- \sigma_b\varepsilon(T)\left(T^4 - T_{amb}^4\right) \tag{1}$$

Fig. 1 – The mesh distribution in the geometric domains.

where P and R denote the laser power and radius of the laser beam, respectively. v, γ, and σ_b represent the scanning speed, heat transfer coefficient, and Stefan−Boltzmann constant. The last two terms (Eq. (1)) represent heat losses by convection and radiation. The temperature-dependent absorptivity $\alpha(T)$ related to the electrical resistivity of the materials and the wavelength of the laser was defined by [41]:

$$\alpha(T) = 0.1457\sqrt{\frac{R_e(T)}{\lambda}} + 0.09 \exp\left(-0.5\sqrt{\frac{\lambda N - 2.1 \times 10^{-6}}{NR_e(T)}}\right) \quad (2)$$

where λ represents the laser wavelength, $R_e(T)$ denotes the electrical resistivity, and N describes the electron layer number of materials. The computational domain was governed by the continuity, momentum, and thermal energy equations, according to [42]:

$$\frac{\partial \rho}{\partial t} + \nabla \cdot (\rho \mathbf{u}) = 0 \quad (3)$$

$$\rho\left[\frac{\partial \mathbf{u}}{\partial t} + (\mathbf{u} \cdot \nabla)\mathbf{u}\right] = \nabla \cdot \left[-p\mathbf{I} + \mu\left(\nabla\mathbf{u} + (\nabla\mathbf{u})^T\right) - \frac{2\mu}{3}(\nabla \cdot \mathbf{u})\mathbf{I}\right]$$
$$- A\frac{(1-F_l)^2}{F_l^2 + B}\mathbf{u} \quad (4)$$

$$\frac{\partial(\rho cT)}{\partial t} + \mathbf{u} \cdot \nabla(\rho cT) = \nabla \cdot (k\nabla T) - \frac{\partial L}{\partial t} - \rho\mathbf{u} \cdot \nabla H \quad (5)$$

where ρ, $\mathbf{u}$, and I denote the density, liquid metal velocity, and identity tensor. c describes the specific heat, k denotes the thermal conductivity, μ and p denote the viscosity and pressure, respectively, while L represents the fusion latent enthalpy, as expressed as $\Delta L = L_h \cdot F_l$, where L_h means the latent heat of the phase transition from solid to liquid. A (2×10^7) in Eq. (4) depends on the porous medium morphology, and B is 1×10^{-3} to avoid dividing by zero [43]. The liquid mass fraction F_l is given by:

$$F_l = \begin{cases} 0, & T < T_s \\ \dfrac{T - T_s}{T_l - T_s}, & T_s \leq T \leq T_l \\ 1, & T > T_l \end{cases} \quad (6)$$

The boundary condition of the liquid/gas momentum equation is given by [39]:

$$F_{L/G} = \sigma\mathbf{n}\kappa - \nabla_s T\frac{d\sigma}{dT} \quad (7)$$

where σ, $\mathbf{n}$, and κ denote the surface tension, normal, and curvature of the free surface, respectively. To track the dynamic shape of the molten pool surface, two interface movement velocities, i.e., the molten pool flow velocity and the interface moving velocity caused by mass addition, were considered the arbitrary Lagrangian−Euler (ALE) moving mesh-based approach [44], which was expressed as

$$V_{L/G} = \mathbf{u} \cdot \mathbf{n} + \mathbf{V_c} \cdot \mathbf{n} \quad (8)$$

where $\mathbf{V_c}$ represents the interface moving velocity due to the deposited powders and is governed by

$$\mathbf{V_c} = \frac{2V_m\eta}{\rho_r\pi R_c^2}\exp\left[-2\frac{(x - vt)^2 + y^2}{R_c^2}\right]\mathbf{z} \quad (9)$$

(3) The molten metal consisted of a composite mixed with the matrix and deposited material during melting. Assuming that this composite mixed adequately in the molten pool, the thermophysical properties of the liquid metal could be determined by [45]:

$$W_m = F_pW_p + F_sW_s \quad (10)$$

where W_m, W_s, and W_p indicate the thermophysical parameters of the simulated molten pool, substrate, and raw materials, respectively, while F_p and F_s denote the volume fractions of the deposited materials and substrate in the molten pool, respectively. Table 2 lists the properties of the Ti811 alloy and deposited materials [46,47].

(4) The deposited powders melted immediately as they entered the molten pool, and only the powders that entered the molten pool contributed to the growth of the deposited track.

3. Experimental section

3.1. Materials and experimental procedures

The Ti811 alloy was selected as the sample. The substrate was sandblasted before the laser cladding process to remove the surface oxides and impurities. A 4-kW TruDisk 4002 laser was

Table 2 − Thermophysical properties of the substrate and raw material powder [31,32].

Name	Ti811	TC4	Ni60	NiCr−Cr$_3$C$_2$
Density (kg m^{-3})	4350	4000	4190	6000
Solidus temperature (K)	1970	1878	1083	1400
Liquidus temperature (K)	2000	1928	1300	1800
Viscosity (Pa s)	2.4×10^{-3}	4×10^{-3}	64×10^{-3}	8×10^{-2}
Specific heat capacity (J kg^{-1} K^{-1})	550	514	120	500
Thermal conductivity (W m^{-1} K^{-1})	7.3	6.5	15	24
Coefficient of thermal expansion (10e^{-6} 1/K)	9	9	13.4	10.9
Latent heat of fusion (KJ/kg)	351	286	250	700
Surface tension coefficient (N/m)	1.6	1.6	1.2	0.5

Table 3 – Laser processing parameters and powder materials system.					
P (W)	V (mm/min)	V_s(Ar)	V_c(He)	D (mm)	Powders composition (wt.%)
900	400	11	7	φ3	65TC4 + 20Ni60 + 15NiCr–Cr$_3$C$_2$
Remarks: P (laser power); V (scanning speed); V_s (shielding gas flow rate); V_c (carrier gas flow rate); D (spot diameter).					

employed to fabricate the coating, where a laser beam with a wavelength of 1030 nm and focal distance of 16.0 mm formed a 3.0 mm diameter circular beam spot on the substrate surface. The laser processing parameters and the proportions of the powders used to prepare the samples are displayed in Table 3. After the laser cladding processing, the metallographic samples were cut by wire electro-discharge machining and prepared according to the standard mechanical polishing method.

3.2. Sample characterization

The phase compositions of the samples were analyzed by X-ray diffraction (XRD, Bruker) analysis with Cu Kα (target) radiation with an operating voltage of 40 kV and a current of 150 mA. The sample microstructures were observed by scanning electron microscopy (SEM, Merlin compact, Zeiss, Germany) equipped with an energy dispersive X-ray spectrometer (EDS, Oxford, Germany). The electron backscatter diffraction (EBSD) analysis sample was prepared by the ion polishing method at 6.5 V for 30 min to meet the testing requirements. The microstructure and interfacial structures were characterized by high-resolution transmission electron microscopy (HRTEM) using a Talos F200X (FEI Corp., USA) at an accelerating voltage of 200 kV. The TEM specimens were prepared by a focused ion beam (FIB) device (Helios Nanolab 600i, Fei Co., USA).

The nanoindentation tests were carried out by a well-calibrated Berger indenter (G200, Agilent, USA), which indented the specimens to a depth of 1000 nm at a strain rate of 0.05 nN/s. The distance between each test point was 200 μm, and at least 10 indentations were used to obtain the hardness values and elastic moduli of the coatings. Wear test samples with dimensions of 10 × 10 × 10 mm (length × width × height) were prepared using a multifunctional wear tester (Retc Instruments, USA), while the WC balls with diameters of 9.5 were selected as the friction pairs, which were applied with a load value of 50 N, frequency of 15 Hz, and test time of 210 s.

4. Results and discussion

4.1. Heat transfer characteristics

Based on the simulation model, the heat transfer and convection of the molten pool could be calculated. Fig. 2 indicates the time-varying simulated temperature field of the molten pool during the deposition process. The arrow represents the velocity distribution, and the cyan and yellow lines represent the solid and liquid phase lines. In the initial stage (10 ms), there was no evident flow because the temperature was below the liquidus temperature (with a maximum of 1740 K), and the

convection velocity was marginal (with a maximum of 1.77×10^{-3} m/s), as shown in Fig. 2(a). Subsequently, the temperature of the irradiated area increased rapidly at 100 ms, and the maximum temperature reached 2690 K, which exceeded the liquidus temperatures of all the deposited powders and the substrate, providing the primary conditions for the deposition process, as shown in Fig. 2(b). In this situation, heat conduction dominated the heat transfer process, resulting in a teardrop-shaped molten pool and deposition of the deposited coating.

Fig. 2(c)–(f) display that the Marangoni effect became stronger with increasing temperature. As the flow fully developed, the maximum fluid velocity reached 0.33 m/s. At this moment, the heat transfer in the molten pool was dominated by Marangoni convection, where the liquid metal flowed from the center to the edge of the molten pool, which enhanced the heat transfer in the molten pool. Finally, the molten pool was stable after 600 ms. The maximum temperature of this stable molten pool was higher than the liquidus temperatures of the deposited powders and the substrate, which ensured the in-situ synthesis of the reinforcements. Moreover, the molten pool shape captured by the coaxial charge-coupled device (CCD) camera at 1000 ms showed an almost identical profile to that of the simulated molten pool, as shown in Fig. 2(g) and (h), indicating that the simulation model was reasonable and credible.

Fig. 3(a) displays the maximum temperature evolution curve of the calculated molten pool at different times, indicating a sharp increase within 1000 ms and stabilization at around 2730 K during subsequent processing. The inset shows a cross-section of the simulated coating compared to the coating obtained after deposition. The high degree of agreement demonstrated the accuracy of the simulation model, which was consistent with the analysis results in Fig. 2(g and h). For simplicity, areas A, B, and C in the coating were considered to be the upper, middle, and bottom areas, respectively. When the temperature and velocity of the simulated molten pool reached a steady state, the temperature and velocity curves at 600 ms, along the laser scanning velocity direction, were obtained, indicating that the temperature had a Gaussian distribution near the laser beam. Due to the effects of temperature and negative surface tension temperature coefficient, the liquid metal flowed from the laser beam center to the sides of the molten pool, resulting in a high-velocity distribution on both sides and a relatively low value in the middle area [33]. In addition, the strong Marangoni convection (0.31 mm/s) caused the liquid metal to circulate before solidification, which promoted the uniform distribution of the elements. Chen et al. [48] obtained the effective moving distance (24.08 mm) and recycling times (6.67 times) of the metal liquid in the molten pool through the three-dimensional model of the laser cladding coating, which proved the sufficient diffusion of solute atoms. Therefore, the
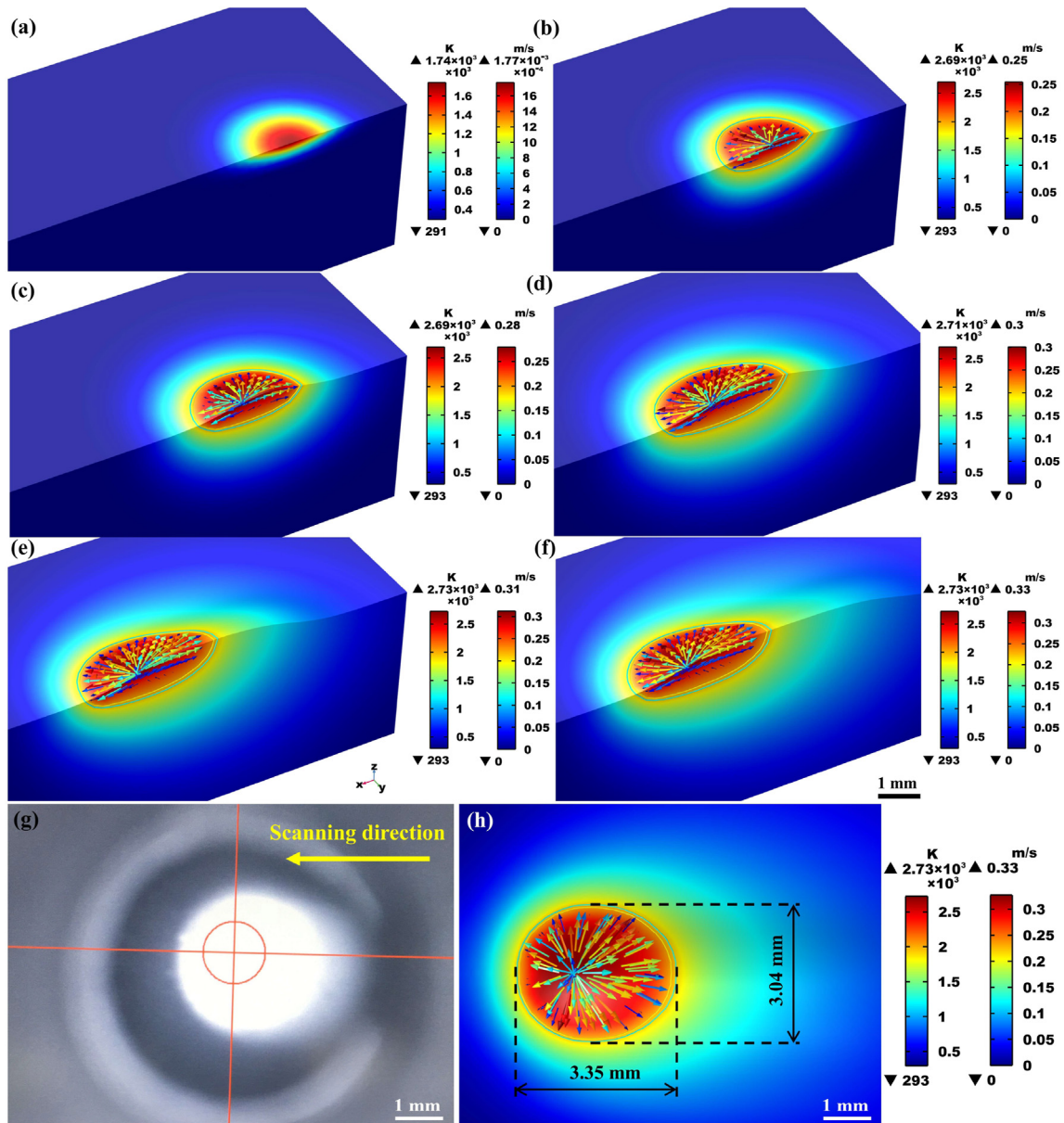
Fig. 2 — Temperature and velocity evolution of the simulated molten pool: (a) 10 ms; (b) 100 ms; (c) 200 ms; (d) 400 ms; (e) 600 ms; (f) 800 ms; (g) comparison of the molten pool monitored by coaxial CCD camera and (h) the model at 1000 ms.

geometry and life of the molten pool were calculated to evaluate the effective moving distance of the molten metal and the number of convection cycles. Fig. 2(h) illustrates that the steady-state melt pool was nearly elliptical, with long- and short-axis lengths of 3.35 and 3.04 mm, respectively. Consequently, the circumference of the molten pool was approximately 10.2 mm. As shown in Fig. 3(b), the laser scanning distance was 3.2 mm when the temperature exceeded the liquidus line (2000 K) of the substrate. Based on the laser scanning speed ($V = 400$ mm/min), the molten pool life was approximately 480 ms. Moreover, according to the molten pool velocity (0.31 m/s), the effective moving distance and number of cycles of the metal liquid were determined to be approximately 148.8 mm and 15, respectively, which ensured sufficient diffusion of the solute atoms.

4.2. Phase composition

The phase-type and microstructure of the deposited coating were critical indicators for determining its mechanical properties. The SEM photographs and XRD results of the raw materials are shown in Fig. 4(a)–(f), showing that oxides and other impurities were not detected in the powders with spherical morphologies and particle sizes from 20 to 100 μm, indicating excellent purity. As shown in Fig. 4(g), the XRD patterns indicated that the coating contained a β solid solution of $CrTi_4$ (space group Im-3m (229), PDF#65-6818) [49], Ti_2Ni as an intermetallic compound (space group Fd-3m (227), PDF#18-0898) [50], and a TiC ceramic-reinforced phase (space group Fm-3m (225), PDF# 32-1383) [51], which confirmed the complete melting of the mixed powders and the presence of
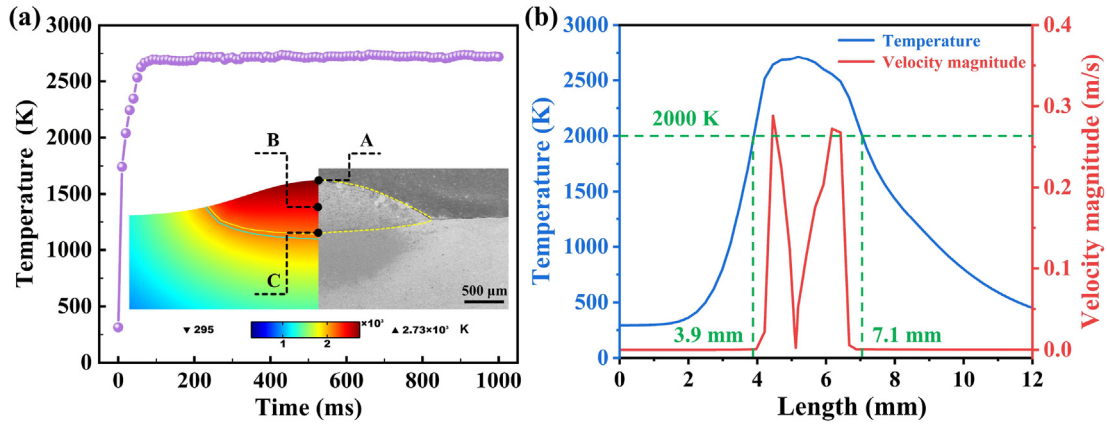
Fig. 3 − (a) Maximum temperature evolution curve along the laser scanning direction, the inset indicates the simulated coating cross-section comparison image, with a high degree of agreement demonstrating the accuracy of the simulated model; (b) temperature and velocity curve along laser scanning direction at 600 ms.

synthesized reinforcements in the deposited coating. Combined with the simulation results, it can be concluded that the high temperature of the laser cladding pool guaranteed the formation of the deposited coating.

EBSD analysis was performed further to identify the microstructures in different coating areas, as shown in Fig. 4(h)−(j). Fig. 4(h)−(h1) demonstrate the band contrast (BC) and BC+phase images of the upper area of the coating, indicating that the coating consisted of a matrix phase (CrTi$_4$), an equiaxed crystal phase (TiC), and a grain boundary precipitation phase (Ti$_2$Ni), which was consistent with the XRD analysis results. Fig. 4(i)−(i1) illustrate the BC and BC+phase images for the middle area of the deposited coating. The difference in phases from the upper area was that the TiC in the middle area exhibited a dendritic state, and a low content α-Ti was observed, indicating that a β−α transition occurred during the solidification of the molten pool. The α-Ti phase could not be detected by XRD analysis due to its small quantity (0.6%). Fig. 4(j) shows the BC image of the coating zone (CZ), bonding zone (BZ), and heat-affected zone (HAZ) of the coating. Combined with the BC+phase image in Fig. 4(j1), the smooth curve (bonding line) indicated the coating was well bonded to the Ti811 substrate. Furthermore, the rapid cooling characteristic of the deposited process resulted in the formation of acicular martensite below the bonding line. Meanwhile, cellular crystals appeared vertically above the bonding line, which is typical of solidified structures for laser cladding. The kernel average misorientation (KAM) method based on the deviation of orientation angle between pixels reflects the local micro-deformation and defect density to evaluate the stress state. The BC+KAM maps in Fig. 4(h2), (i2), and (j2) show that the green aggregation appears at the grain boundaries, demonstrating that considerable residual stress existed due to the large temperature gradient (G) and cooling rate (R) during laser processing. Notably, the insets in Fig. 4(h) and (i) showed that the mean sizes (equivalent circle diameter) of the phases were 5.6 and 5.9 μm, respectively. Based on the microstructural characteristics of the upper and middle areas in the coating, this phenomenon was caused by the different solidification characteristics of each area in the deposited coating.

Solidification characteristics analysis of the molten pool in Section 4.3 can reasonably explain this phenomenon.

4.3. Solidification characteristics

The temperature distribution of the molten pool significantly affected the solidification behavior of the laser cladding coating. The G and R at the solidification front of the simulated molten pool were the two dominant parameters that affected the solidification structure. Fig. 5 shows the influences of G and R on the morphology and size of the microstructures [52], indicating that a faster cooling rate (G × R) resulted in smaller crystals. Furthermore, the morphological parameter (G/R) of the microstructure determined the morphology. As G/R decreased, the microstructural morphology changed from cellular crystals to dendrites and equiaxed dendrites, where G and R could be defined by [52]:

$$G = \sqrt{\left(\frac{\partial T}{\partial x}\right)^2 + \left(\frac{\partial T}{\partial y}\right)^2 + \left(\frac{\partial T}{\partial z}\right)^2} \tag{11}$$

$$R = V \cdot \cos \theta \tag{12}$$

where θ represents the angle between R and V.

Fig. 6(a) shows the G and R curves at 1000 ms in the X−Z plane based on the calculated transient temperature field results. The results showed that the G value from the upper to the bottom interfaces decreased gradually because of the energy transfer in the molten pool through thermal conduction and convection. Eq. (12) shows that the solidification rate R was positively correlated with cosα. From the upper area to the bottom area of the solidification interface, the value of cosα continuously reduced, resulting in a decrease in R from 6.67 to 0.23 mm/s, a reduction of nearly 30 times. The calculated results are consistent with the previously reported numerical simulation work of related laser cladding processing [48,53,54]. Therefore, the change in the solidification characteristics of the molten pool was mainly dependent on the significant difference in the solidification rate. Fig. 6(b) shows the corresponding relationship between G and R. Combined
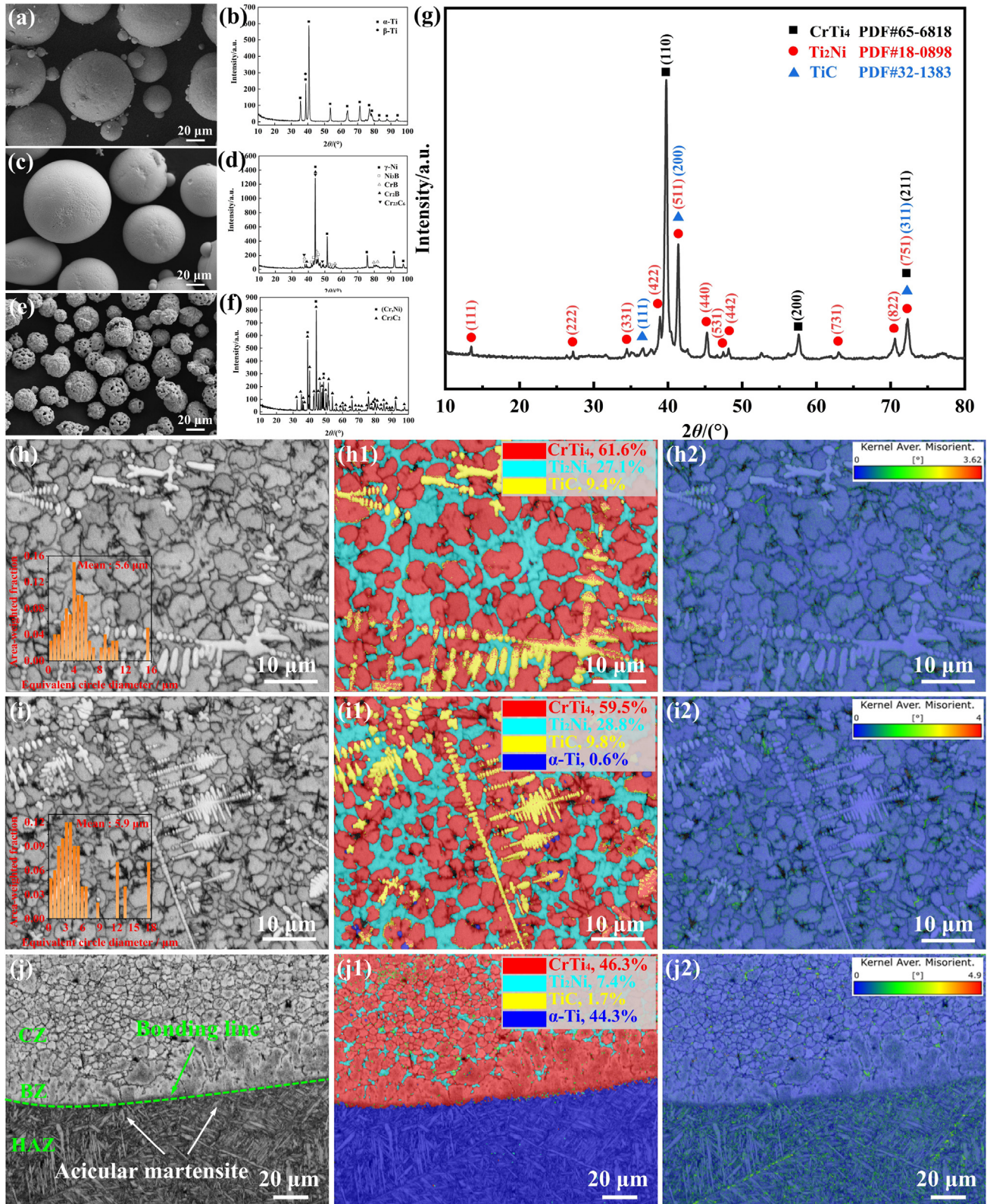
Fig. 4 — SEM photographs and XRD patterns of the (a—b) TC4 powder, (c—d) Ni60 powder, and (e—f) NiCr—Cr$_2$C$_3$ powder; (g) XRD pattern of the coating; EBSD analysis of the region A of the coating: (h) BC image; (h1) BC+Phase image, and (h2) BC+KAM image; the region B of the coating: (i) BC image, (i1) BC+Phase image, and (i2) BC+KAM image; the region C of the coating: (j) BC image, (j1) BC+Phase image, and (j2) BC+KAM image.
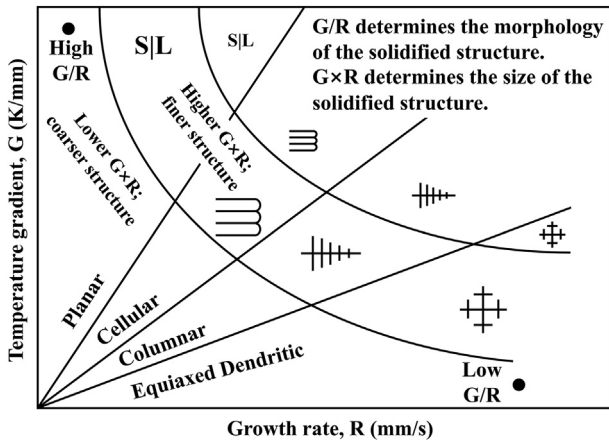
Fig. 5 − Effects of G and R on morphology and size of microstructure [36].

with Fig. 5, the microstructural morphology and scale of the deposited coating could be reasonably predicted.

Therefore, the upper, middle, and bottom areas of the deposited coating were selected to study the differences in the solidification characteristics of the different areas in the coating. The deposited coating was etched by the chemical solution (HNO$_3$:HF:H$_2$O = 1:1: 0, volume ratio) for 20−30 s to study the microstructural evolution by SEM (Hitachi S−3000 N, Japan), as shown in Fig. 7. According to the simulation results, a higher $G \times R$ (8558 K/s) and a lower G/R (192 Ks/mm^2) were obtained for the upper area of the coating. This showed that the microstructure in the upper area of the deposited coating consisted of equiaxed crystals with smaller sizes, as shown in Fig. 7(a) and (b). However, a lower $G \times R$ (130 K/s) and a higher G/R (2457 Ks/mm^2) were calculated for the bottom area of the deposited coating. This indicated that the structure in the bottom area tended to consist of cellular crystals, as shown in Fig. 7(e) and (f). In addition, the values of $G \times R$ (2674 K/s) and lower G/R (137 Ks/mm^2) in the middle area of the coating were located between the upper and bottom areas, and the microstructure was dominated by dendritic crystals, as shown in Fig. 7(c) and (d). Therefore, with a continuous decrease in G/R, the microstructure of the coating gradually transitioned from

cellular crystals in the bottom area to dendrites in the middle area and equiaxed crystals in the upper area.

4.4. Precipitation mechanism

Numerical simulations verify that laser cladding provides the thermodynamic conditions for molten pool formation. As the laser beam moved, the activated molten pool resolidified to synthesize various phases in the deposited coating. To determine the precipitation order of these phases, Fig. 8 shows the relationship between the Gibbs free energy (ΔG) of the reactions and the temperature. The negative ΔG values for all the chemical reactions indicated their spontaneity. Fig. 9 shows the microstructure and phase evolution of the laser cladding process. Under laser irradiation, the surface of the Ti811 alloy melted, and a molten pool dominated by elemental Ti, Cr, Ni, and C was formed. Because Ti is a solid carbide-forming element with a low ΔG for the reaction Ti + C → TiC, the TiC phase formed and precipitated preferentially in the molten pool. As solidification continued, TiC grew as a nucleus by absorbing the surrounding carbon and Ti atoms while simultaneously repelling the Ni atoms. Because of the high cooling rate of the molten pool, the chemical composition in the front portion of the liquid phase was supercooled, causing the dendritic growth of TiC. Due to the high G and R values at the upper area of the deposited coating, the chemical composition at the front of the liquid phase was supercooled, resulting in the growth of TiC as equiaxed crystals. As the G and cooling rate decreased from the upper area to the bottom area of the molten pool, the middle and bottom areas were dominated by dendritic TiC and cellular crystals, respectively. Subsequently, CrTi$_4$ formed when the temperature decreased to approximately 1933 K. With further decreases in temperature, the formation of a carbon-depleted zone at the front of the liquid phase led to the segregation of elemental nickel, which contributed to the formation of the Ti$_2$Ni phase according to the reaction of 2Ti + Ni→ Ti$_2$Ni. Finally, the reinforced phases at room temperature were TiC + CrTi$_4$ + Ti$_2$Ni.

4.5. Interface characteristics

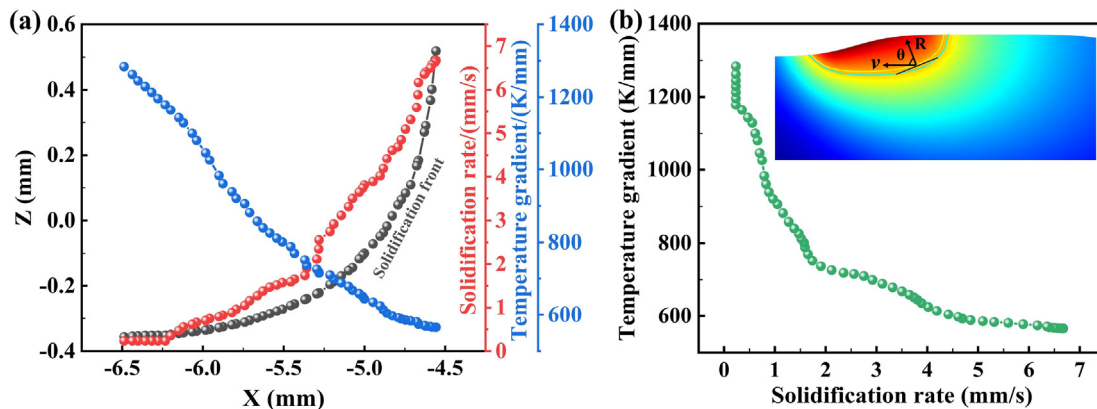The deposited coating contains numerous interfaces, which act as a bridge connecting the reinforced phase and the

Fig. 6 − (a) Calculated G and R of the solidification front; (b) relationship curve between G and R.
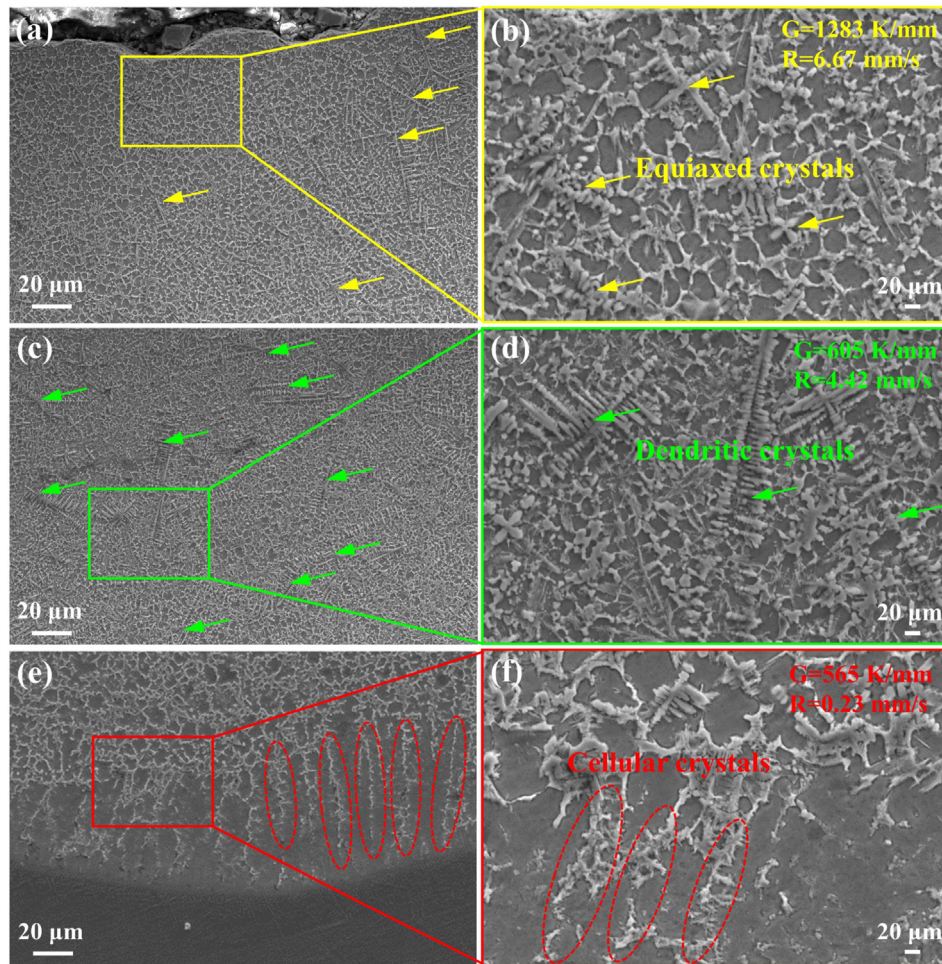
Fig. 7 − SEM photographs of the (a−b) upper, (c−d) middle, and (e−f) bottom areas of the deposited coating.
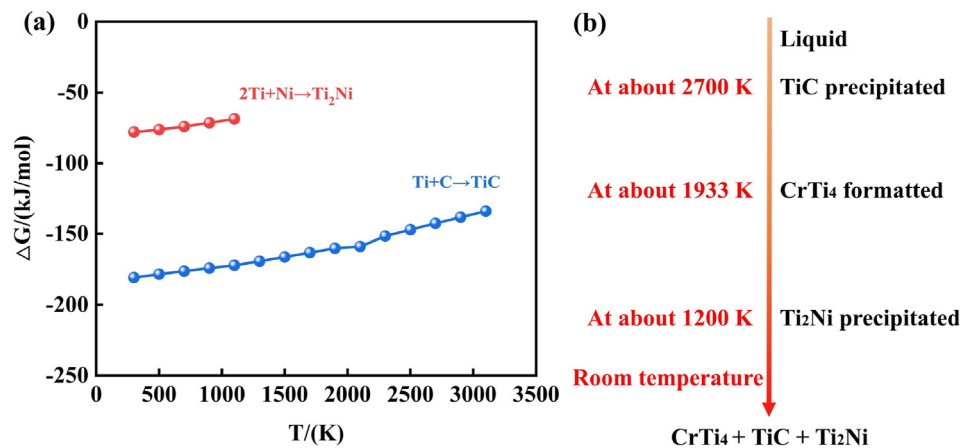

Fig. 8 − Relationship between ΔG and temperature.

substrate, playing an important role in enhancing the mechanical properties of the coating [16,17]. An ideal interface between different phases should be free of cracks and interfacial reactions [55−57]. Consequently, TEM observations were used to explore the interface structure between in-situ phases. Fig. 10(a) indicates the bright-field image of the phase in the upper area of the deposited coating. The EDS maps of Fig. 10(a) are shown in Fig. 10(b)−(e). It is seen that the dark particle phase mainly contains Ti and C elements, the surrounding stripe phase is composed of Ti and Ni elements, and the matrix consists of Ti and Cr elements, which are preliminarily identified as TiC, Ti_2Ni, and $CrTi_4$ phases. Furthermore, dislocations were observed in Fig. 8(a), which can effectively increase the average hardness of the matrix.
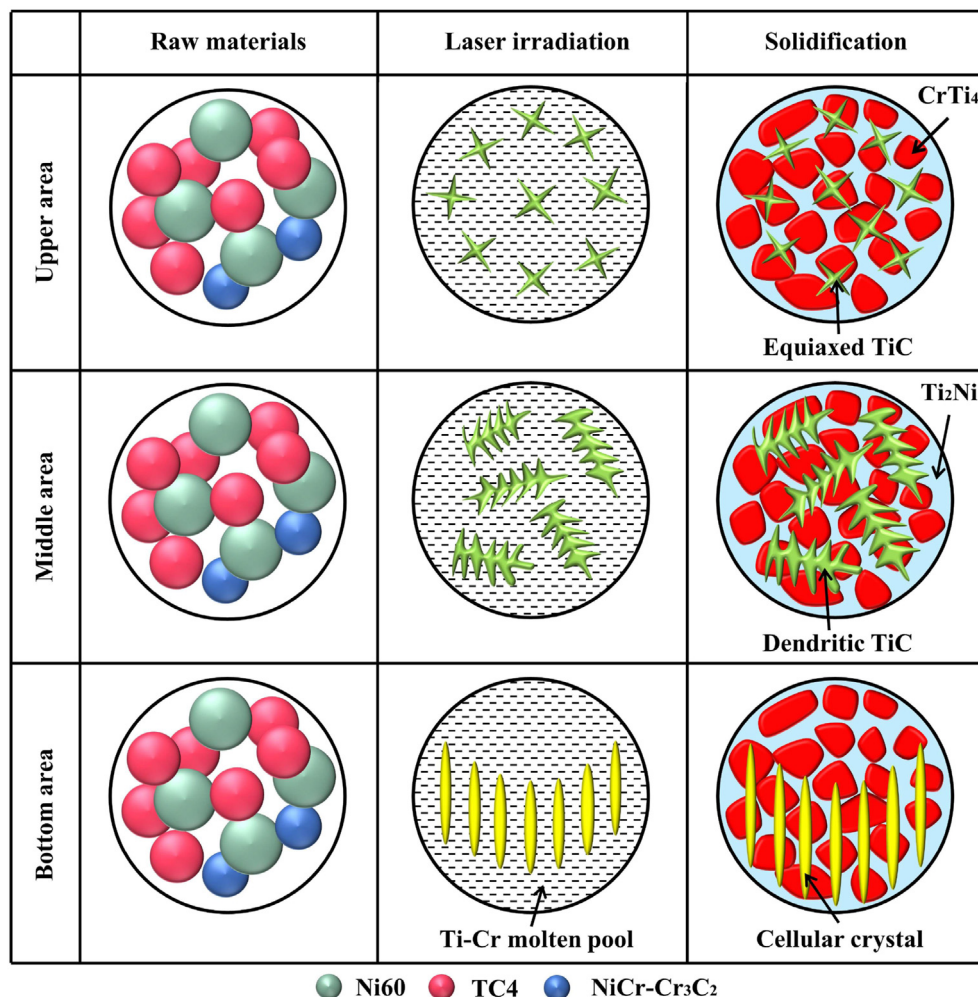
Fig. 9 – Schematic of microstructure and phase evolution of the laser cladding coating.

Fig. 10(f) and (g) show the HRTEM images of the red box f and green box g in Fig. 10(a). The IFFT images in the insets show the atomic structures of TiC, Ti_2Ni, and $CrTi_4$. It is seen that the respective interplanar spacings can be well marked. Combined with the detailed SAED patterns in Fig. 10(h)–(k), it shows that TiC, Ti_2Ni, and $CrTi_4$ belong to the FCC, FCC, and BCC crystal structures, respectively. Meanwhile, the IFFT images in Fig. 10(f) indicate lattice parameters of TiC and Ti_2Ni, which verified the lattice distance of 0.216 nm for TiC(-200) and 0.259 nm for $Ti_2Ni(33\text{-}1)$, demonstrating an approximately parallel relationship (~12°) between TiC(-200) and $Ti_2Ni(33-1)$ planes. The lattice misfit (δ) establishes qualified support for the degree of interfacial bonding and can be calculated according to the following Eq. (13) [25]:

$$\delta = \frac{|d\text{TiC}_4(-200) - d\text{Ti}_2\text{Ni}(33-1)|}{d\text{Ti}_2\text{Ni}(33-1)} = 16.6\% \quad (13)$$

Note that the consistency of high, medium, and low interfaces is defined as the misfit of less than 5%, with the range of 5–25% and more than 25%, respectively. Therefore, one of the orientational relationships between TiC and Ti_2Ni can be expressed as: TiC [001]//Ti_2Ni [-123], TiC(-200)//$Ti_2Ni(33-1)$.

Based on the measured lattice parameters, the misfit dislocation is 16.6%, which was a semi-coherent coherent interface, suggesting a great combination between the TiC phase and Ti_2Ni matrix at the atomic scale.

Furthermore, the detailed SAED patterns in Fig. 10(j and k) clearly show that the $CrTi_4$ [-111] direction consists of (0-11), (101), and (110) planes with an identical interplanar distance of 0.227 nm, while the Ti_2Ni [$5-54$] direction is composed of (220), (-135), and (-315) planes with the interplanar distance of 0.399 nm, 0.190 nm, and 0.190 nm, respectively. The IFFT images in Fig. 10(g) indicate that the $CrTi_4$ (110) plane with the interplanar distance of 0.227 nm is approximately parallel (~10°) to the $Ti_2Ni(-315)$ plane with the interplanar distance of 0.190 nm. It should note that the interface is clean and free of interfacial reactions, making the bonding of the interface quite strong. According to Eq. (13), the calculated misfit between them is 16.3%, which is a semi-coherent interface, and their orientational relationship can be expressed as $CrTi_4[-111]$//Ti_2Ni [$5-54$], $CrTi_4(110)$//Ti_2Ni (-315). It reveals that the TiC/Ti_2Ni and $CrTi_4$/Ti_2Ni interfaces were well-bonded with no interface reactants, indicating that both interfaces had good interfacial compatibility and wettability.
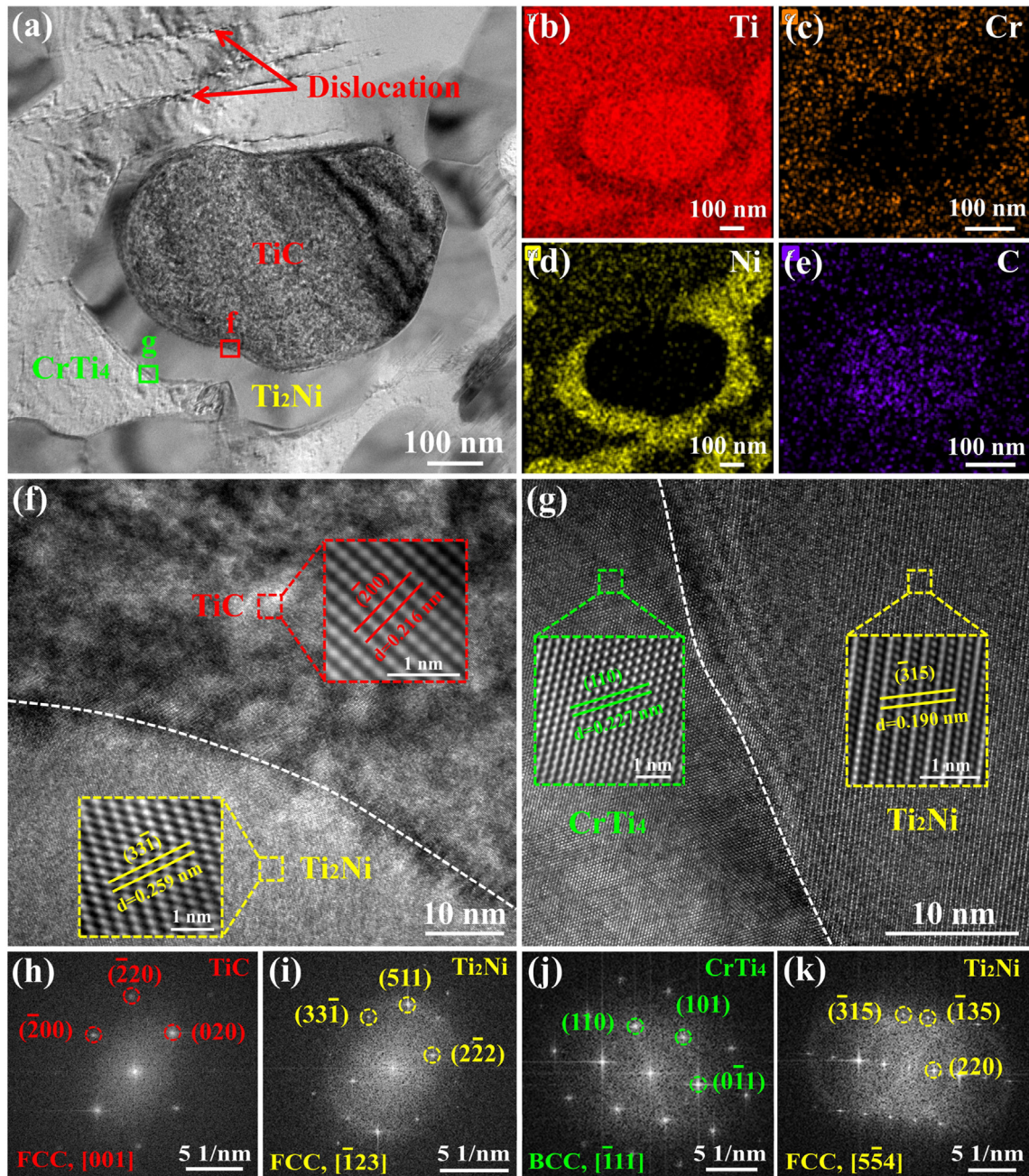
Fig. 10 − TEM characterization of the upper coating. (a) Bright-field image of TiC, Ti_2Ni, and $CrTi_4$; EDS maps of (b) Ti, (c) Cr, (d) Ni, and (e) C elements; (f) HRTEM image of the dashed box f in (a) indicates TiC/Ti_2Ni interface; (g) HRTEM image of the dashed box f in (a) indicates $CrTi_4/Ti_2Ni$ interface; FFT images of (h) TiC and (i) Ti_2Ni in (f); FFT images of (h) $CrTi_4$ and (i) Ti_2Ni in (g).

4.6. Mechanical properties

The indentation images of the deposited coating and Ti811 alloy in Fig. 11(a)−(d) show that the coating possessed a smaller indentation size, where the indentation images of the coatings in Fig. 11(a)−(d) were numbered 1−4. Based on these results and the corresponding load−displacement curves in Fig. 11(e), the deformation resistance of the coating was higher than the substrate under identical test conditions. Fig. 11(f) and (g) showed the hardness and elastic modulus curves corresponding to each indentation. The results showed that

the hardness of the coating was significantly higher than the substrate. These results were consistent with the expectations due to the refined grains produced during the laser cladding process. Elements such as Cr, Al, and V dissolved in the Ti matrix to form the β solid solution ($CrTi_4$), which will cause lattice distortion and help to increase the resistance of dislocation movement, thus making it difficult for the slip to proceed and improving the hardness of the coating. Furthermore, according to the Hall−Petch equation [58], the finer microstructure obtained by laser cladding is beneficial to improving strength. The hardness and elastic modulus values
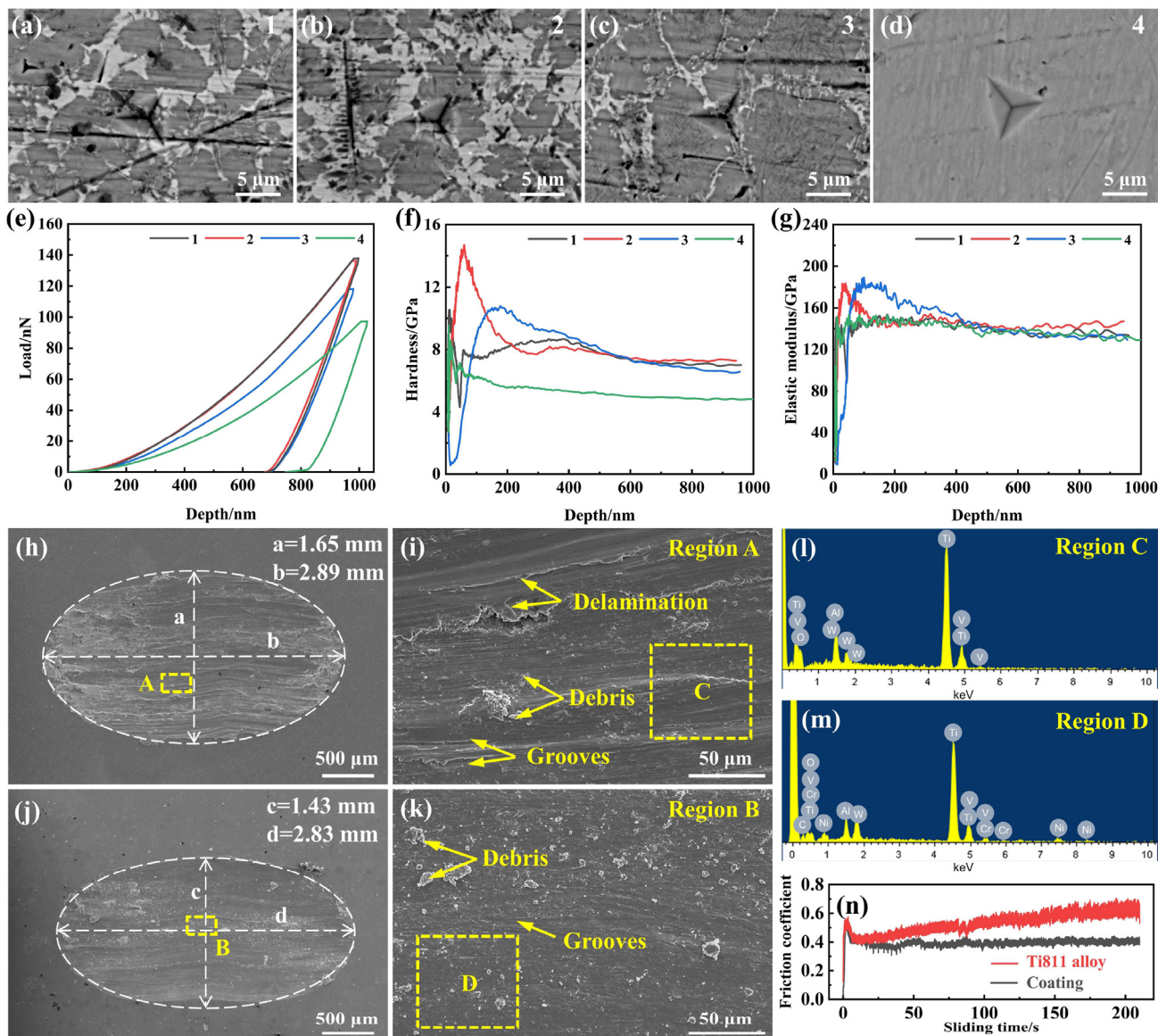
Fig. 11 − Nano-hardness and wear resistance analysis of the deposited coating and the substrate. Nanoindentation morphology of (a) the upper, (b) middle, (c) bottom regions, and (d) Ti811 alloy; (e) load versus indentation depth; (f) nano-hardness and (b) elastic modulus curves of the coating; SEM images after wear tests of (h−i) Ti811 alloy, and (j−k) coating; (l) friction coefficient curve of the Ti811 alloy and coating; EDS analysis results of (m) region C, and (n) region D.

of the coating were approximately 7.41 GPa and 142 GPa, respectively, which were 1.54 and 1.08 times greater than those of the substrate (4.8 GPa and 132 GPa, respectively). This is caused by the combined effects of solid solution strengthening and grain refinement strengthening [16].

Excellent friction and wear properties ensure the service performance of coatings in harsh environments. Fig. 11(h) and (j) show the elliptical wear morphologies of the Ti811 alloy and coating, respectively. The lengths of the long and short axes of the deposited coating were less than the substrate length, indicating its enhanced wear resistance. The magnified SEM image of the substrate in Fig. 11(i) shows that the surface of the substrate with relatively low hardness was very rough after wear, with deep grooves, chips, and severe deformation. During the wear process, the WC balls, with high hardness,

easily penetrated the substrate, resulting in the large plastically deformed materials removal and abrasive particles formation. As the sliding time increased, the particles exhibited a microchipping effect on the substrate, resulting in the construction of deep ravines. Based on these results and EDS analysis of areas C and D in Fig. 11(l) and (m), the elemental W was attributed to the interactions with the WC balls. Therefore, the wear mechanisms of the Ti811 alloy were mainly dominated by adhesive and abrasive wear. However, as shown in Fig. 11(k), the coating surface after the wear test was relatively smooth with shallow grooves and a small amount of debris. During the wear process, the evenly distributed reinforcing phase in the coating could effectively resist the intrusion of the WC balls, improving the wear resistance of the coating. Fig. 11(n) shows the coefficient of friction values of

the deposited coating and the Ti811 alloy as a function of sliding time. The friction coefficient of the Ti811 alloy was extremely unstable throughout the wear process, ranging from 0.42 to 0.6, resulting in a gradually increasing trend. However, the friction coefficient of the coating stabilized after 80 s and remained in the range of 0.38—0.42. The stable coefficient of friction benefited from the high hardness of the coating and the uniform distribution of the in-situ reinforcement phase. The relatively smooth surface after the wear test improved the friction curve smoothness. Significantly, the robust interfaces between the reinforcing phases and the dislocations in the matrix guaranteed the improved mechanical properties of the coating. Therefore, the wear mechanisms were dominated by abrasive and slight adhesive wear.

5.   Conclusions

In this work, surface deposited coatings were prepared on a Ti811 alloy by coaxial powder-feeding laser cladding technology. A simulation model of the coupling of multiple physical fields in the laser cladding process was established to reveal the heat transfer and solidification characteristics of the molten pool and the formation mechanisms of the in-situ phases. The main conclusions were summarized as follows.

1. The simulation results demonstrated that the stable temperature field of the molten pool ensured the formation of the in-situ phases and the growth of the deposited coating. Strong Marangoni convection resulted in outward flow from the center of the molten pool, and the effective distance and number of convection cycles were 148.8 mm and 15, respectively, which improved the uniform distribution of elements.

2. Thermodynamic calculations determined the precipitation order of the reinforced phase as $TiC \rightarrow CrTi_4 \rightarrow Ti_2Ni$, where the low ΔG of the TiC ceramic phase led to its preferential precipitation. The formation of the $CrTi_4$ matrix was attributed to the abundant Ti and Cr elements, and the Ti_2Ni intermetallic compounds tended to precipitate between the grain boundaries.

3. Compared to the bottom area of the deposited coating, the G and R values at the upper area increased by 2.27 times and 29 times, respectively. The microstructure showed an evolution trend from cellular crystals to dendrites and then to equiaxed crystals from the bottom area to the upper area of the coating.

4. The nano-hardness of the deposited coating was 1.89 times higher than the substrate, which is attributed to the solid solution strengthening effect, the dispersion strengthening effect of the reinforcing phase, the robust interfacial bonding between phases, and the existence of dislocations. The coefficient of friction of the coating was in the range of 0.38—0.42, which was approximately 30% lower than that of the substrate. The formation of the in-situ reinforcement phase caused the wear mechanism of the coating to be dominated by slight adhesive and abrasive wear.

Declaration of Competing Interest

The authors declare that they have no known competing financial interests or personal relationships that could have appeared to influence the work reported in this paper.

Acknowledgments

REFERENCES

[1] Alabort E, Barba D, Shagiev MR, Murzinova MA, Galeyev RM, Valiakhmetov OR, et al. Alloys-by-design: application to titanium alloys for optimal superplasticity. Acta Mater 2019;178:275—87.

[2] Zhang D, Qiu D, Gibson MA, Zheng Y, Easton MA. Additive manufacturing of ultrafine-grained high-strength titanium alloys. Nature 2019;576(7785):91—5.

[3] Li W, Cao C, Yin S. Solid-state cold spraying of Ti and its alloys: a literature review. Prog Mater Sci 2020;110:100633.

[4] Lin Z, Song K, Yu X. A review on wire and arc additive manufacturing of titanium alloy. J Manuf Process 2021;70:24—45.

[5] Zhang J, Li X, Xu D, Yang R. Recent progress in the simulation of microstructure evolution in titanium alloys. Prog Nat Sci: Mater Int 2019;29(3):295—304.

[6] Singh G, Ramamurty U. Boron modified titanium alloys. Prog Mater Sci 2020;111:100653.

[7] Bhardwaj T, Shukla M, Paul CP, Bindra KS. Direct energy deposition - laser additive manufacturing of titanium-molybdenum alloy: parametric studies, microstructure and mechanical properties. J Alloys Compd 2019;787:1238—48.

[8] Chi J, Cai Z, Zhang H, Zhang H, Guo W, Wan Z, et al. Combining manufacturing of titanium alloy through direct energy deposition and laser shock peening processes. Mater Des 2021;203:109626.

[9] Pouzet S, Peyre P, Gorny C, Castelnau O, Baudin T, Brisset F, et al. Additive layer manufacturing of titanium matrix composites using the direct metal deposition laser process. Mater Sci Eng, A 2016;677:171—81.

[10] Zhao T, Zhang S, Zhou FQ, Zhang HF, Zhang CH, Chen J. Microstructure evolution and properties of in-situ TiC reinforced titanium matrix composites coating by plasma transferred arc welding (PTAW). Surf Coating Technol 2021;424:127637.

[11] Cassar G, Banfield S, Avelar-Batista Wilson JC, Housden J, Matthews A, Leyland A. Impact wear resistance of plasma diffusion treated and duplex treated/PVD-coated Ti—6Al—4V alloy. Surf Coating Technol 2012;206(10):2645—54.

[12] An Q, Chen J, Tao Z, Ming W, Chen M. Experimental investigation on tool wear characteristics of PVD and CVD coatings during face milling of Ti6242S and Ti-555 titanium alloys. Int J Refract Metals Hard Mater 2020;86:105091.

[13] Vlcak P, Fojt J, Weiss Z, Kopeček J, Perina V. The effect of nitrogen saturation on the corrosion behaviour of Ti-35Nb-7Zr-5Ta beta titanium alloy nitrided by ion implantation. Surf Coating Technol 2019;358:144—52.

[14] Zhu L, Xue P, Lan Q, Meng G, Ren Y, Yang Z, et al. Recent research and development status of laser cladding: a review. Opt Laser Technol 2021;138:106915.

[15] Weng F, Chen C, Yu H. Research status of laser cladding on titanium and its alloys: a review. Mater Des 2014;58:412–25.

[16] Arif ZU, Khalid MY, ur Rehman E, Ullah S, Atif M, Tariq A. A review on laser cladding of high-entropy alloys, their recent trends and potential applications. J Manuf Process 2021;68:225–73.

[17] Liu J, Yu H, Chen C, Weng F, Dai J. Research and development status of laser cladding on magnesium alloys: a review. Opt Laser Eng 2017;93:195–210.

[18] Rajan TPD, Pillai RM, Pai BC. Reinforcement coatings and interfaces in aluminium metal matrix composites. J Mater Sci 1998;33:3491–503.

[19] Zhao Y, Zhao Q, Xia M, Chen H, Liu X. Unveiling the semicoherent interface with definite orientation relationships between reinforcements and matrix in novel Al_3BC/Al composites. ACS Appl Mater Interfaces 2016;8(41).

[20] Feng Y, Feng K, Yao C, Li Z. Effect of LaB_6 addition on the microstructure and properties of $(Ti_3Al + TiB)/Ti$ composites by laser cladding. Mater Des 2019;181:107959.

[21] Liu P, Sun D, Han X, Wang Q. Investigation on the crystallographic orientation relationships and interface atomic structures in an in-situ $Ti_2AlN/TiAl$ composite. Mater Des 2017;130:239–49.

[22] Song X, Cui H, Han Y, Ding L, Song Q. $Ti_2Al(C, N)$ solid solution reinforcing TiAl-based composites: evolution of a core-shell structure, interfaces, and mechanical properties. ACS Appl Mater Interfaces 2018. acsami.8b02023.

[23] Zhang N, Han X, Sun D, Liu H, Wu G. Crystallographic orientation relationships and interfacial structures between reinforcement and matrix phases in an in situ $(Ti, Nb)B/Ti_2AlNb$ composite. Appl Surf Sci 2021;542:148592.

[24] Liu X, Nuhfer NT, Rollett AD, Sinha S, Lee SB, Carpenter JS, et al. Interfacial orientation and misorientation relationships in nanolamellar Cu/Nb composites using transmission-electron-microscope-based orientation and phase mapping. Acta Mater 2014;64:333–44.

[25] F. Wang, J. Li, C. Shi, E. Liu, C. He, N. Zhao.. Orientation relationships and interface structure in $MgAl_2O_4$ and $MgAlB_4$ Co-reinforced Al matrix composites. ACS Appl Mater Interfaces 2019;11(45):42790–800.

[26] Zheng SJ, Ma XL, Yamamoto T, Ikuhara Y. Atomistic study of abnormal grain growth structure in $BaTiO_3$ by transmission electron microscopy and scanning transmission electron microscopy. Acta Mater 2013;61(7):2298–307.

[27] Zhang MX, Kelly PM, Easton MA, Taylor JA. Crystallographic study of grain refinement in aluminum alloys using the edge-to-edge matching model. Acta Mater 2005;53(5):1427–38.

[28] Feng H, Zhou Y, Jia D, Meng Q, Rao J. Growth mechanism of in situ TiB Whiskers in spark plasma sintered TiB/Ti metal matrix composites. Cryst Growth Des 2006;6(7):1626–30.

[29] Hu D, Liu Y, Chen H, Liu J, Wang M. Effect of TiC addition on the microstructure and properties of Ni_3Ta–TaC reinforced Ni-based wear-resistant coating. Ceram Int 2021;47(16):23194–202.

[30] Kooi BJ, Pei YT, Hosson J. The evolution of microstructure in laser clad TiB–Ti composite coating. Acta Mater 2003;51(3):831–45.

[31] Liu Y, Ding Y, Yang L, Sun R, Zhang T, Yang X. Research and progress of laser cladding on engineering alloys: a review. J Manuf Process 2021;66:341–63.

[32] Chen L, Yu T, Xu P, Zhang B. In-situ NbC reinforced Fe-based coating by laser cladding: simulation and experiment. Surf Coating Technol 2021:127027.

[33] Wang C, Zhou J, Zhang T, Meng X, Li P, Huang S. Numerical simulation and solidification characteristics for laser cladding of Inconel 718. Opt Laser Technol 2022;149:107843.

[34] Li C, Yu Z, Gao J, Zhao J, Han X. Numerical simulation and experimental study of cladding Fe60 on an ASTM 1045 substrate by laser cladding. Surf Coating Technol 2018;357:965–77.

[35] Tamanna N, Crouch R, Naher S. Progress in numerical simulation of the laser cladding process. Opt Laser Eng 2019;122:151–63.

[36] Liu G, Zhang X, Chen X, He Y, Cheng L, Huo M, et al. Additive manufacturing of structural materials. Mater Sci Eng R Rep 2021;145:100596.

[37] DebRoy T, Wei HL, Zuback JS, Mukherjee T, Elmer JW, Milewski JO, et al. Additive manufacturing of metallic components – process, structure and properties. Prog Mater Sci 2018;92:112–224.

[38] Hu Y, He X, Yu G, Ge Z, Zheng C, Ning W. Heat and mass transfer in laser dissimilar welding of stainless steel and nickel. Appl Surf Sci 2012;258(15):5914–22.

[39] He X, Song L, Yu G, Mazumder J. Solute transport and composition profile during direct metal deposition with coaxial powder injection. Appl Surf Sci 2011;258(2):898–907.

[40] Qi H, Mazumder J, Ki H. Numerical simulation of heat transfer and fluid flow in coaxial laser cladding process for direct metal deposition. J Appl Phys 2006;100(2). 24903-24903-11.

[41] (translated from Russian by R.B. Rodman) Infrared radiation – a handbook of applications M.A. Bramson. 1971.

[42] Theoretical analysis and model experiments on the formation mechanism of channel-type segregation. Trans Iron Steel Inst Jpn 1978;18(2):90–8.

[43] Asai S, Muchi I. Theoretical analysis and model experiments on the formation mechanism of channel-type segregation. Trans Iron Steel Inst Jpn 1978;18(2):90–8.

[44] Morville S, Carin M, Peyre P, Gharbi M, Fabbro R. 2D longitudinal modeling of heat transfer and fluid flow during multilayered. J Laser Appl 2013;24:32008–11. 9.

[45] Wei HL, Liu FQ, Wei L, Liu TT, Liao WH. Multiscale and multiphysics explorations of the transient deposition processes and additive characteristics during laser 3D printing. J Mater Sci Technol 2021;77:196–208.

[46] Liu FQ, Wei L, Shi SQ, Wei HL. On the varieties of build features during multi-layer laser directed energy deposition. Addit Manuf 2020;36:101491.

[47] Gramberg U. In: Alloys-preparation, properties, applications. vol. 314. Weinheim: F. Habashi (HRSG.) Wiley-VCH; 1998. Seiten, geb., DM 298, ISBN 3-527-29591-7, Chemie Ingenieur Technik.

[48] Chen L, Yu T, Xu P, Zhang B. In-situ NbC reinforced Fe-based coating by laser cladding: simulation and experiment. Surf Coating Technol 2021;412:127027.

[49] PROLA, Transactions of the American society for metals (ASM).

[50] The crystal structures of Ti_2Cu, Ti_2Ni, Ti_4Ni_2O, and Ti_4Cu_2O. Trans Aime 1963;227.

[51] Becker K, Ebert F. Die Kristallstruktur einiger binrer Carbide und Nitride. Z Phys 1925;31(1):268–72.

[52] Gan Z, Yu G, He X, Li S. Numerical simulation of thermal behavior and multicomponent mass transfer in direct laser deposition of Co-base alloy on steel. Int J Heat Mass Transfer 2017;104:28–38.

[53] Wang C, Zhou J, Zhang T, Meng XK, Li P, Huang S. Numerical simulation and solidification characteristics for laser cladding of Inconel 718. Opt Laser Technol 2022;149:107843.

[54] Li C, Yu Z, Gao J, Zhao J, Han X. Numerical simulation and experimental study of cladding Fe60 on an ASTM 1045 substrate by laser cladding. Surf Coating Technol 2018;vol. 357.

[55] Liu Z, Zhao D, Wang P, Yan M, Yang C, Chen Z, et al. Additive manufacturing of metals: microstructure evolution and multistage control. J Mater Sci Technol 2022;100:224−36.

[56] Pelz JS, Ku N, Meyers MA, Vargas-Gonzalez LR. Additive manufacturing of structural ceramics: a historical perspective. J Mater Res Technol 2021;15:670−95.

[57] Gong G, Ye J, Chi Y, Zhao Z, Wang Z, Xia G, et al. Research status of laser additive manufacturing for metal: a review. J Mater Res Technol 2021;15:855−84.

[58] Hansen N. Hall−Petch relation and boundary strengthening. Scr Mater 2004;51(8):801−6.